

Using Fiber Optic Bundles to Miniaturize Vision-Based Tactile Sensors

Julia Di^{1,2}, Zdravko Dugonjic^{3,4}, Will Fu¹, Tingfan Wu², Romeo Mercado², Kevin Sawyer², Victoria Rose Most², Gregg Kammerer², Stefanie Speidel^{4,5,6}, Richard E. Fan¹, Geoffrey Sonn¹, Mark R. Cutkosky¹, Mike Lambeta², and Roberto Calandra^{2,3,6}

Abstract—Vision-based tactile sensors have recently become popular due to their combination of low cost, very high spatial resolution, and ease of integration using widely available miniature cameras. The associated field of view and focal length, however, are difficult to package in a human-sized finger. In this paper we employ optical fiber bundles to achieve a form factor that, at 15 mm diameter, is smaller than an average human fingertip. The electronics and camera are also located remotely, further reducing package size. The sensor achieves a spatial resolution of 0.22 mm and a minimum force resolution 5 mN for normal and shear contact forces. With these attributes, the DIGIT Pinki sensor is suitable for applications such as robotic and teleoperated digital palpation. We demonstrate its utility for palpation of the prostate gland and show that it can achieve clinically relevant discrimination of prostate stiffness for phantom and *ex vivo* tissue.

Index Terms—perception for grasping and manipulation, force and tactile sensing, fiber optics, tissue palpation, robotic palpation, medical robotics, object hardness, deep learning in robotics.

I. INTRODUCTION

FOR robot hands to substitute human hands in tasks requiring tactile acuity, they should match the force and spatial resolution of human fingertips while also having comparable stiffness and dimensions. Towards this goal, we present a novel approach for miniaturizing vision-based tactile sensors by using fiber bundles as optical conduits, and demonstrate its use for manipulation tasks in constrained settings that cannot be done with larger fingers.

Tactile spatial resolution matching or even exceeding that of the human fingertip has recently become possible using vision-based sensors. Popular examples include the DIGIT [1], GelSight [2], and TacTip [3] sensors, which use miniature cameras to capture the deformation of a transparent elastomer gel and apply machine learning techniques to estimate the associated surface deformation and stresses. These examples, however, are relatively large compared to human fingertips, chiefly due to the need to meet the optical path requirements of an internal

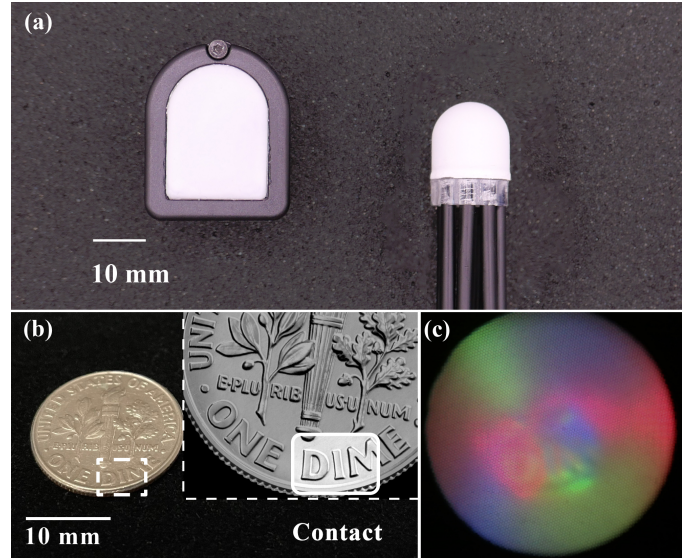


Figure 1: (a) DIGIT [1] (left) compared with the DIGIT Pinki (right) introduced in this work. The DIGIT Pinki's diameter of 15 mm is achieved using optical fiber bundles as illumination and imaging conduits, thereby allowing the elastomer sensing element to achieve human scale. (b) At just 15 mm, the diameter of DIGIT Pinki's sensing element is smaller than the standard U.S. dime (17.9 mm); (c) the raw image of the DIGIT Pinki pressed against the "DIME" portion, with its sub-millimeter structure visible.

camera. Several researchers have recently proposed slimmer designs to address this issue, but it remains a challenge to produce designs that match the geometry of a human fingertip. For example, the GelSlim 3.0 [4] and Gelsight Wedge [5], while slim, lack a rounded three-dimensional sensing surface. Meanwhile, dome-shaped, three-dimensional sensors such as OmniTact [6], GelSight360 [7], and Insight [8] have base diameters of 30 mm, 28 mm, and 40 mm respectively. At the size of a large adult thumb or toe, they are not a direct substitute for a human fingertip. Moreover, it is difficult to miniaturize them further due to the focal length and field of view of the camera, and the desire to package the camera and all associated electronics, including illumination, in the base.

Slim and sensitive fingertips in the size range of the smallest adult human fingers unlock the kinds of manipulation tasks that cannot be done with larger fingers. One potentially life-saving example is cancer detection, through the tissue

¹ Stanford University, Stanford, CA, USA {juliadi, jiaxiang, refan, gsonn, cutkosky}@stanford.edu

² Authors affiliated at time of work with Meta, Menlo Park, CA, USA {romeo12, kevin.sawyer, tingfan, victoriainmost, greggk, lambetam}@meta.com

³ LASR Lab, Technische Universität Dresden, Germany

{zdugonjic, rcalandra}@lasr.org

⁴ School of Embedded and Composite AI (SECAI)

⁵ National Center for Tumor Diseases (NCT/UCC) Dresden

{stefanie.speidel}@nct-dresden.de

⁶ Centre for Tactile Internet with Human-in-the-Loop (CeTI)

palpation of internal cavities during remote or teleoperated exams. In particular, prostate cancer is the fifth leading cause of cancer death in men worldwide but can be detected early with regular screening protocols including the digital rectal examination (DRE), in which the prostate area is gently palpated with a gloved finger through the rectum [9]. Although the exam is easy to perform, the result is subjective and depends on the experience of the examiner [10]. A robotic care provider, perhaps controlled remotely, could provide objective and quantitative measurements if equipped with a slim and sensitive tactile fingertip.

Motivated by the problem of palpation in internal cavities and similarly constrained environments, we present a design approach that can miniaturize vision-based tactile sensors to match average human fingertips, shown in Fig. 1. At 15 mm, the diameter of the DIGIT Pinki is no larger than an average female index fingertip or a 5th percentile male fingertip [11]. Inspired by early fiber-based imaging research, we use optical fiber bundles as conduits for illumination and imaging, allowing the separation of the sensing element from supporting circuitry.

Because the supporting circuitry and processing are located remotely, the sensor size is no longer constrained by the base and the optical path for the internal camera, lens, and lighting. Instead, the primary constraint is the bundle size, as determined by the desired resolution and lighting requirements.

In presenting this new design, our contributions are:

- the design, fabrication, and testing of an optical tactile sensor that uses optical fiber bundles to match human fingertip dimensions and approach human tactile sensitivity;
- an optical system design that integrates fibers for imaging and illumination and a distal lens to achieve a wide field of view in a hemispherical dome;
- a demonstration of the suitability of the sensor for medical palpation and an ability to provide clinically relevant levels of tissue stiffness discrimination.

To encourage further experimentation with the presented technology we are also open-sourcing the hardware design at <https://github.com/facebookresearch/digit-design>.

II. RELATED WORK

A. Vision-Based Tactile Sensors

In recent years, camera technology has improved significantly, becoming smaller, cheaper, and higher in resolution. Such improvements have opened up new implementations of tactile sensors that cast tactile sensing as a computer vision problem—learning or modeling tactile features or properties from high-resolution images captured by a camera. When combined with significant progress in computer vision and machine learning, these new high-resolution vision-based sensors are promising for tactile perception.

A prevailing design paradigm for vision-based tactile sensors involves the use of an optically-transparent elastomer, a camera, and a lighting system. These types of sensors then image the indentation an object makes on the elastomer at the point of contact, thereby capturing surface property information as a tactile image. The information can include the texture,

contact area, forces, contact centroid, and other computed tactile features that may then be used for manipulation.

To better suit dexterous manipulation tasks, recent works have developed these sensing designs from planar to a three-dimensional. One common form factor that has emerged is an elastomer gel shaped in a hemisphere or dome, reminiscent of a human fingertip that may then be mounted on a robotic finger. OmniTact [6], GelTip [12], and GelSight360 [7] are all recent examples of these fingertip vision-based tactile sensors. Another common theme is that of a slim elastomer gel for direct integration with a gripper, with elastomers shaped as wedges [4], finrays [13], or fingers themselves [8], [14].

Despite the differences in elastomer shapes, all of these sensors either house the camera internally at the base of the sensor, or use an arrangement of mirrors or prisms which direct light to an internal camera located a short distance away. Further miniaturization of the sensing element may prove challenging with these existing designs, which leads us to investigate a different design solution using optical fiber bundles.

B. Fiber-Based Tactile Sensing

Fiber-based sensors have a long history in applications requiring some or all of the following considerations: small size, light weight, immunity to electromagnetic radiation, or an ability to transfer information over long distances [15], [16]. In particular, optical fiber bundles are widely used for light delivery and, in the case of coherent fiber bundles (CFBs), direct image delivery as well. Both coherent and incoherent fiber bundles have been used in borescopes and endoscopes for decades, allowing access to the smallest vessels of the human body [17], [18]. These characteristics, and the ready availability of high-quality coherent fiber bundles, recommend them for lighting and image delivery in our application.

We note also that the general idea of imaging through fiber-based optical waveguides has already been explored in early vision-based tactile sensors, in part because camera miniaturization was not yet mature [19]–[21]. A seminal example from 1988 involved a finger-shaped optical tactile sensor where an optical fiber waveguide conveyed a tactile image to a charge-coupled device (CCD) camera [22]. In this design, each fiber is attached to a transducer membrane along a hemispherical surface, and the tactile image is created when an object scatters light at the contact point due to frustrated internal reflection (FTIR). A drawback to the FTIR approach is that some of the details of the contact image are lost in order to enhance the contrast between contacting and non-contacting areas. More recent sensors with fiber-based conduits have also exploited FTIR but pose challenges for manufacturing at scale (e.g. [23]) or provide a substantially lower resolution (e.g., [24], [25]) than what is available from modern cameras.

In this work, we revisit the idea of fiber-based tactile sensing through the lens of endoscopic design principles to achieve high spatial resolution with small sensor size. Modern incarnations of flexible fibreoptic endoscopes often employ a proximal video camera for image capture through the CFB [17], or use a miniature CCD chip at the distal end of a flexible shaft, with

incoherent optical fiber bundles to deliver diffuse white-light illumination from the proximal to distal end [26]. Both designs result in a slim imaging scope, with trade-offs between size and resolution. While previous research in fiber-based imaging has investigated optical techniques (e.g., imaging relay and scanning mechanisms [27], fiber characterization [28], and case studies in medicine [29], [30]), we do not know of works that extend these design details to the system level needed for integration into vision-based tactile sensors. Such details include the arrangement of fibers and lighting for a hemispherical elastomer dome and the design of a miniature distal lens for imaging at close range with high field of view.

C. Tactile Applications in Medicine

Tactile sensing has been explored for a number of applications in medicine. In the realm of minimally invasive surgeries, tactile feedback systems enhance precision by providing surgeons with a sense of touch [31]–[33]. Other researchers have used tactile feedback systems to improve robotic manipulation tasks, such as automatic swab sampling [34], [35]. Tactile sensors also are useful as diagnostic tools, for instance in the classification of tissue mechanical properties for patient examination [36]–[38].

In this work we demonstrate the benefits of DIGIT Pinki’s small size in a medical palpation case study of the prostate gland. Over a million men receive a prostate cancer diagnosis each year, with many physicians routinely screening via the digital rectal exam (DRE) [39]. In the DRE, a physician inserts a gloved finger to probe the lower rectum, dynamically palpating for any abnormalities in the prostate gland. Because around 80% of prostate cancers arise in the posterior region [40], which is palpable via the readily-available and inexpensive DRE, it continues to be recommended for clinical practice in addition to more advanced biomarker, imaging, or biopsy diagnostic tools [41].

Nevertheless, because the DRE and similar palpation examinations are widely accepted as *subjective* measurements, researchers have investigated ways to quantify them with sensorized robotic systems. To mimic the DRE, some researchers have affixed a probe to a force-torque sensor for palpation case studies, or have used fibers with Fiber Bragg Gratings (FBGs) for strain sensing [42]–[44]. Others have investigated robotic palpation classifiers for breast and prostate tumors [45], [46]. None of these investigations has demonstrated a high-resolution vision-based tactile sensor small enough to be clinically relevant for the DRE and similarly constrained manipulation tasks.

III. DESIGN AND FABRICATION

In this section we detail the design principles and corresponding choices made during the design of the DIGIT Pinki. We additionally describe how each of the components of the sensor works, and present their manufacturing process.

A. System Design

We identified three primary requirements to guide the design:

- small elastomer sensing element with diameter and stiffness comparable to a human fingertip,
- high spatial resolution for computer vision,
- high field of view across the curved fingertip area.

Based on these requirements, we explored design details for the elastomer gel and interface, the illumination via fibers, and the imaging via fibers. For the proof-of-concept prototype, we constructed a prototype that is 15 mm in diameter, which is shown in Fig. 2. As noted earlier this makes DIGIT Pinki approximately the size of an adult female index fingertip or a fifth percentile male fingertip [11]. Furthermore, as discussed in Section VII, the design can in principle be reduced to just a few millimeters in diameter.

B. Elastomer Gel

DIGIT Pinki uses a deformable elastomeric material in the shape of a hemispherical dome atop a short cylindrical section. A detailed manufacturing guide and open-source resources can be found on <https://github.com/facebookresearch/digit-design>.

A hemispherical gel acts as an integrating sphere for light rays, so a fully Lambertian scattering surface reduces indentation contrast compared to a Gaussian scattering surface [47]. Therefore, to control the light scattering at the surface, we machined a metal mold with a smooth and polished surface and then finely sandblasted the surface to achieve a precise texturing. We also found alternatively that one may cast a dome-shaped daughter mold with Mold Star or a similar mold-making silicone and vary the amount of mold release used on the mold in order to achieve a similar texturing, though with less consistency than the machined mold. Once a mold was prepared for casting, Smooth-On Solaris (Shore 10A), an optically clear silicone, was syringed into the mold cavity. We vacuum degassed the silicone while in the mold to ensure that no air bubbles were present. All samples are cured for 24 hours at room temperature.

There are two layers on the elastomer gel dome: a reflective layer and a protective layer over the reflective layer. After demolding, the gel dome was cleaned with 99% isopropyl alcohol, and airsprayed with a thin layer of Inhibit-X and then left to outgas for 30 minutes at room temperature. Then we sprayed Rustoleum Mirror Effect paint until the surface is evenly coated with a reflective layer. This was followed by a thin layer of Inhibit-X to prepare the surface for the protective layer. To make the protective layer, we mixed Ecoflex 00-10 in a ratio of 1:1 Part A to Part B, with an additional 1% white Smooth-on Silc Pig by weight. The mixture was then diluted with 4% by weight of NOVOCS matte. The mixture is vacuum degassed and then drizzled onto the reflective layer in a process akin to drip candy coating. This drip process took only a few minutes and was much faster than airspraying silicone, a fabrication technique in other work that can take hours, or painting with a small brush. The resulting thin layer of protective Ecoflex 00-10 silicone was fully cured after 4 hours. At this point, the elastomer gel dome was ready to use.

C. Illumination

With the proposed fiber-based approach, DIGIT Pinki used plastic optical fibers coupled to LEDs for illumination rather

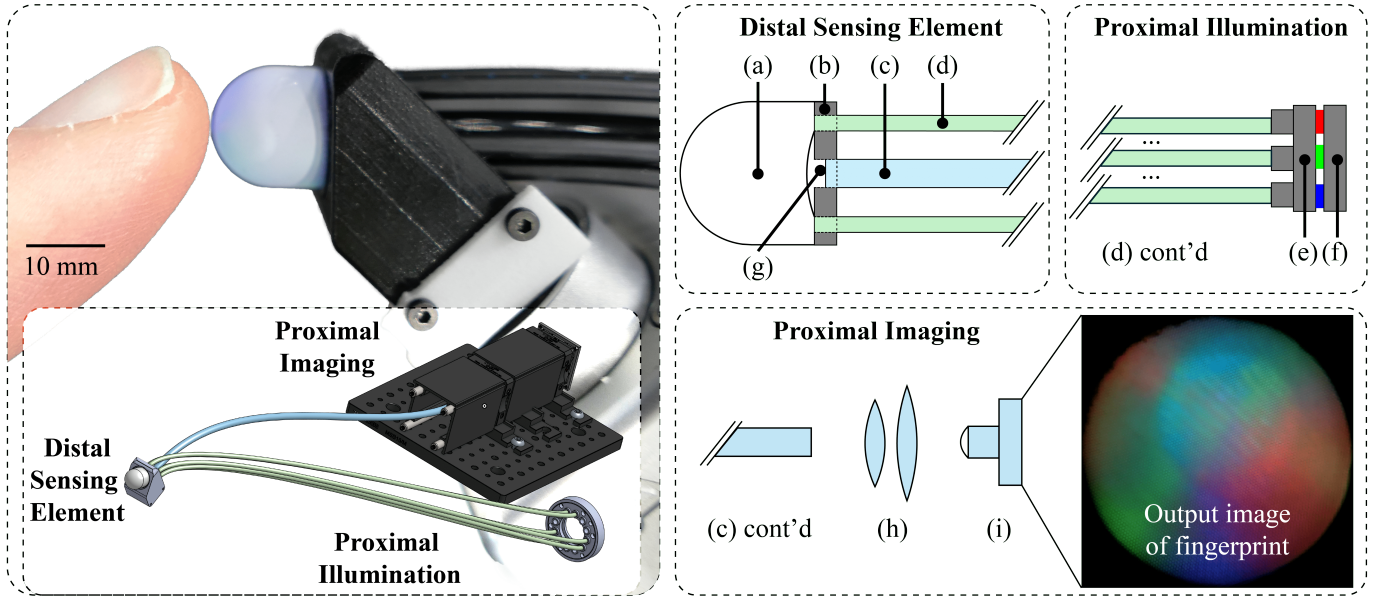


Figure 2: The proposed system consists of: a distal sensing element, a proximal imaging system, and a proximal illumination system, all of which are connected with optical fiber bundles. The distal end contains (a) an elastomer gel mounted in (b) a 3D-printed housing (pictured at left is a housing compatible with the Allegro Hand, but this housing could be designed for other uses). Both the (c) imaging and (d) illumination fiber bundles mate to the gel. At the proximal end, the illumination fiber bundles mate to the (e) collimator coupled to (f) LEDs. When making contact with an object (e.g. a woman's index finger), the gel is first imaged with (g) a distal hyperfisheye lens, conveyed through the imaging fiber bundle, then magnified by (h) optical lenses and captured by the (i) camera. The proximal imaging and illumination systems may be co-located or separate.

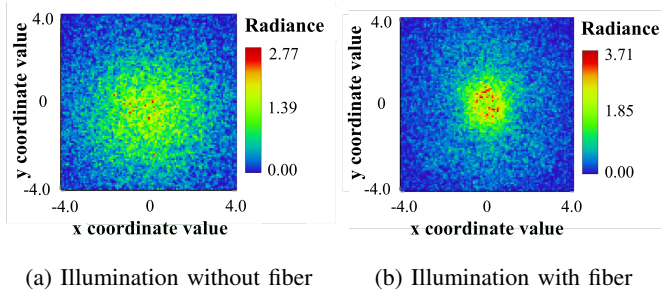


Figure 3: Comparison of the ray-traced outputs in Zemax Optics Studio of lighting from a 5050 RGB LED package (a) without and (b) with the fiber bundle. The fiber output is narrower and more focused.

than LEDs directly. The light source we used in this prototype is an Adafruit Neopixel ring with 5050 RGB LEDs, which is a Lambertian source according to the manufacturer radiation diagram. We then directly coupled each LED package to a 48-core incoherent plastic optical fiber bundle, with end faces that were manually polished using 200, 400, and 1000 grit sandpaper. The bundles were directly coupled to the elastomer gel dome and held with a 3D-printed housing (Fig. 2).

Consideration was given to the location of the illumination fibers relative to the base of the elastomer gel dome. We defined their placement to the elastomer gel with these parameters: number of fiber bundles n_b , radius of each fiber bundle (inclusive of any jackets) r_f , the radial distance between the center of each bundle from sensor center r_b , and angular

spacing between bundles α_b . We empirically found that while 3 was a minimal number of bundles (for RGB illumination), 6 fiber bundles equally spaced at 5.75 mm radius r_b worked better.

Some important design parameters when choosing a fiber-based illumination conduit are the core diameter c_d and the numerical aperture of the fiber NA . These parameters help characterize both how much light is relayed through the bundle and the output light profile from the bundle.

We wanted to minimize the light loss through the fiber bundles. We chose a 3 mm diameter incoherent fiber bundle to minimize geometry-based coupling loss with the LEDs while maintaining a small overall diameter at the sensing element. We also used an index-matched gel when optically coupling to minimize Fresnel loss. Therefore, any light loss in our system is largely angular coupling loss, which can be estimated. Based on Lambert's cosine emission law, $I(\theta) = I_0 \cos \theta$, we can calculate the angular coupling loss as

$$\eta_{ang} = \sin^2 \theta_{fiber}^2, \quad (1)$$

where the fiber acceptance angle is $\theta_{fiber} = \arcsin(NA)$. For the proof of concept prototype in this work, we calculated a 25% loss due to angular acceptance coupling loss. For any future prototypes that use much longer fibers, the loss calculation should include attenuation loss. The fiber used in DIGIT Pinki has a 0.65 dB/m attenuation rating, but because the fibers used in this prototype are only about 0.4 m in length, we ignored attenuation loss for this case. Fiber system light loss may also be partially compensated for by varying the intensity of the input LEDs.

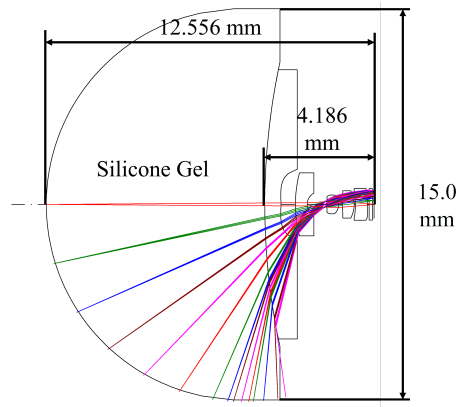


Figure 4: Custom distal hyperfisheye lens design for a 15 mm diameter dome-shaped silicone gel. The lens design has 5 components and provides a 192° field of view.

One result from using fiber bundles for lighting is that the output light profile is different from a Lambertian diffuse source. To study this, we modeled in Zemax Optics Studio a comparison between the 5050 LED package without fibers and with the 3 mm diameter PMMA fiber bundle as a lighting conduit (Fig. 3). In this model, we plotted the ray-traced light intensity received at a rectangular detector 3 mm away from the light source using 1,000 analysis rays for both scenarios. We found that illumination through a fiber bundle is more narrow in output compared to the Lambertian light source of a direct LED. We then approximated the lighting as a Gaussian beam instead of a Lambertian source, with a cone of light given by the numerical aperture (NA) of the fiber bundle. Less uniform illumination is not necessarily disadvantageous; while hotspots may saturate the image sensor more quickly, reducing the maximum detectable deformation, they can also increase imaging contrast for perceiving fine features.

D. Imaging

We chose the IMX298 16MP Arducam camera with a pixel size of $1.12 \times 1.12 \mu\text{m}$ and a maximum image resolution of 4656×3496 pixels when imaging at 10 Hz, though the frame rate is adjustable up to 30 Hz at lower resolutions. The camera parameters such as brightness, white balance, and exposure are also adjustable.

For imaging through a fiber bundle, the effective spatial resolution is most often constrained by the fiber packing density and fiber core diameter, rather than the camera sensor and imaging optics. Resolution in this case refers to the minimum feature dimensions that can be resolved with a modular transfer function (MTF) ≥ 0.5 . In the proof of concept, we used a 7400-core imaging fiber bundle made of Poly (methyl methacrylate) plastic, which was packed as a hexagonal array in a 2 mm diameter polyethylene jacket and had a individual fiber core of 0.2 mm.

To achieve a high field of view of the hemispherical gel, a wide-angle lens is necessary at the distal end of the fiber. Most existing vision-based tactile sensors use a commercial off-the-shelf camera module with a M12 wide angle lens, but these lenses are too wide for our purposes.

Thus, we designed a custom compact hyperfisheye lens for the DIGIT Pinki, as shown in Fig. 4, which provided a 192° field of view. This custom lens was optimized for tactile sensing input in a dome-shaped sensor. In comparison to commercially-available lenses intended for photography, we were relatively unconcerned about optical distortions. Therefore the lens intentionally allowed chromatic aberrations and removed anti-reflective coatings to capture reflection and scattering inside the elastomer. The design used APEL 5014 plastic material and could be manufactured either by diamond turning or a molding process.

Due to resource constraints, we were unable to manufacture the hyperfisheye lens design in time for testing. Therefore, for tests described in the next section, we only image the tip (60° field of view) with a non-hyperfisheye distal lens. The spatial resolution result reported in Section IV is with the 60° lens, but the same resolution with the hyperfisheye lens could be attained by increasing the fiber core count accordingly.

E. Assembly

We assembled our prototype, as pictured in Fig. 2, in the following manner.

First, we prepared the distal end of the sensor. We bonded a completed gel to a thin 3D-printed thread using Smooth-On Sil-Poxy Silicone Adhesive. Once cured, we then were able to screw the gel onto a corresponding 3D-printed gel housing. A few gel housing configurations were designed during prototyping, but for all reported experiments in the next section we used a 3D-printed housing compatible with the fingertip of an Allegro hand. Other vision-based tactile sensors typically overmold the gel elastomers directly onto a base PCB or skeleton frame, but we found that a “screw-on” gel allowed for easier swapping of gel tips, which is especially useful for medical applications. Of note is that this modularity is in part enabled by the fiber design, where the camera and other sensitive opto-electronics are packaged remotely, so swapping a gel only involves unscrewing the old gel, reapplying an index-matched optical gel, and screwing a new gel back on.

In the prototype, we used a MEDIT, Inc. fiber bundle containing 7,400 cores and a 60° distal lens for the imaging conduit, and a 48-core incoherent optical fiber bundle for the illumination conduit. These illumination and imaging fiber bundles were directly coupled to the gel with an index-matched optical gel (Cargille 0608), and adhered with cyanoacrylate to the gel housing from the opposite side.

Next, we prepared the proximal end of the sensor, consisting of the proximal illumination and imaging systems. The illumination and imaging systems may be co-located, but in the prototype built in this work they were separated for modularity.

For the illumination system, the illumination fibers were adhered with cyanoacrylate to a 3D-printed collimator, which was directly coupled to a 12-LED Adafruit Neopixel ring mounted in an LED holder. The illumination fibers have minimum bend radius of 75 mm before light leakage occurs, so we ensured during operation that the fibers stay within the acceptable bend radius to prevent further light loss.

To image the proximal end face of the imaging fiber bundle, we set up an optical bench system with ThorLabs components.

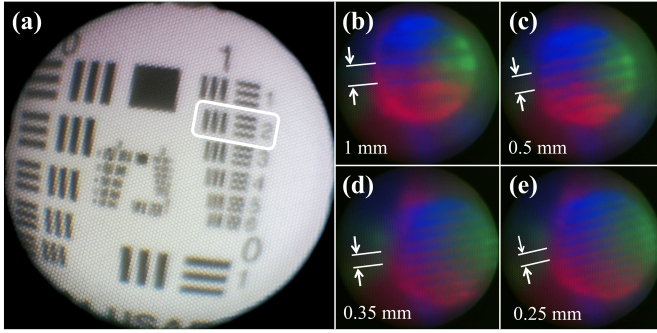


Figure 5: (a) The USAF 1951 Test Pattern resolution target as captured with the imaging fiber (no gel). The working distance is set to the height of the gel. Group 1, element 2, which is outlined in white, can still be resolved (lines do not blur). When zoomed in to the output image, there is an apparent “honeycomb” pattern, as is typical when imaging through fibers. (b-e) Readings from a DIGIT Pinki when pressed against machined calibration blocks with known line widths of: (b) 1 mm, (c) 0.50 mm, (d) 0.35 mm, and (e) 0.25 mm. The indentations of the lines are visible.

Table I: Comparison between DIGIT and DIGIT Pinki

Sensor	Sensing Area (mm ²)	Sample Rate (Hz)	Spatial Resolution (mm)	Normal Force Resolution (N)	Shear Force Resolution (N)
DIGIT	304	60	0.150	0.006	0.012
DIGIT Pinki	1,404*	10**	0.22	0.005	0.005

* This number is from the proposed hyperfisheye lens design.

** Sampling rate at highest resolution of 4656×3496 pixels. A 30 Hz sampling rate is available at lower resolutions (1920×1080 pixels).

All pieces were mounted to an optical breadboard, which we set up with a 30 mm adjustable optical cage and light shields. From the imaging fiber bundle, we aligned an adjustable diopter, a 10x Plan microscope objective, and a microscope eyepiece to a 16MP IMX298 USB camera connected to a computer.

In Appendix A we provide the CAD for this assembly, and in Appendix B we provide the materials and components.

IV. SENSOR CHARACTERIZATION

This section describes the characterization results for the DIGIT Pinki in terms of spatial resolution and normal and shear force estimation. We also provide an analytic validation of the contact patch evolution using contact mechanics theory.

A. Spatial Resolution

To verify the resolution of the sensor system optics, we used a standard United States Air Force (USAF) resolution target as commonly used for microscopes and cameras. This benchtop test is a tri-bar test, where the optical resolution of the system is determined by assessing the visibility of groups of bars. The resolution is the smallest group where all three black bars can be separated. The image from the

Table II: Results for Normal and Shear Force Estimation

Dataset	Indenter	RMSE ± STD (mN)
Normal	4 mm	3.7 ± 3.2
	12 mm	3.9 ± 3.7
	Flat	3.5 ± 2.9
Normal (10k)	4 mm	8.2 ± 7.4
	12 mm	6.9 ± 5.6
	Flat	6.6 ± 6.5
Shear	4 mm	5.0 ± 3.3
	12 mm	3.8 ± 2.5
	Flat	6.5 ± 4.0
Shear (10k)	4 mm	5.3 ± 2.6
	12 mm	6.6 ± 2.3
	Flat	5.6 ± 3.0

USAF resolution target test captured through the fiber bundle is shown in Fig. 5a with a working distance equal to that at the tip of the gel. We clearly observed Group Number 1, Element Number 2, for a resolution of 2.24 lines per mm. Based on this resolution test target, the DIGIT Pinki can resolve a line width of approximately 222.72 μm. The true resolution limit is between 222.72 μm and 198.43 μm (which corresponds to Element Number 3). Note that this resolution limit is for a system using the 60° distal lens and 7,400-core imaging fiber; changes to either optical components could improve the resolution limit.

We also tested the resolution of imaging through an elastomer gel. To do so, we custom machined a calibration test target block. The block has line widths of 1.00 mm, 0.5 mm, 0.35 mm, and 0.25 mm. The results from this test are shown in Fig. 5b-e. The camera exposure in this sequence is set to −1. The indentations of the lines are clearly visible down to 0.25 mm.

B. Normal and Shear Force Estimation

We assess force estimation by evaluating DIGIT Pinki’s ability to measure applied normal and shear forces at a contact. Because we are motivated by a tissue palpation use case, or other similar fine manipulation, we are primarily interested in the ability to measure light forces up to 1 N.

We used an indenter to probe DIGIT Pinki’s sensing element. As shown in Fig. 6a, we mounted the DIGIT Pinki on a Mecha robotic arm, and installed the metal indenter probe on a force sensor on top of a linear stage. During this process of contacting the surface, we collected images of the surface under contact and the contact force vectors from a force sensor embedded under the indenter. We used three different indenter probe tips: 4 mm diameter, 12 mm (on the order of the size of the sensor tip), and a flat metal surface (larger than the sensor tip). The variety in tip sizes produces different contact loading conditions.

We collected two types of datasets: normal and shear.

1) *Normal Force Dataset*: To characterize normal force performance, we used a single-axis force sensor under the indenter probe. For a point on the tip of DIGIT Pinki, the probe pressed perpendicularly into DIGIT Pinki until the normal force of the force sensor crosses a threshold of 1 N. During contact, the measured normal force and DIGIT Pinki images

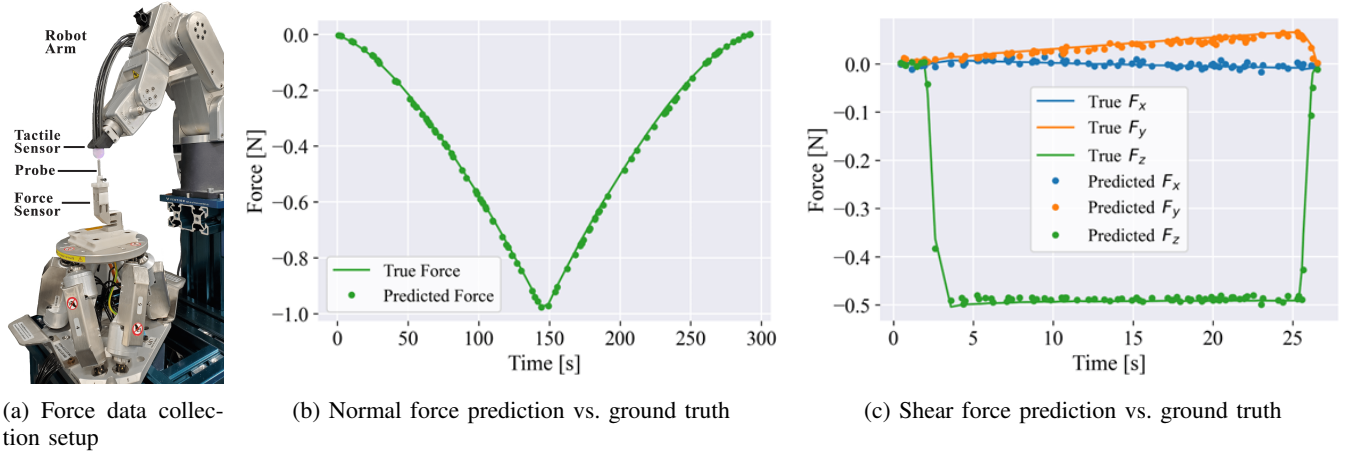


Figure 6: (a) Benchmarking setup used to collect force data over three different indenter types. From the dataset we train the image-to-force prediction models. (b) We plot the predicted force compared to ground truth for one indentation in the normal force dataset from 0 N to -1 N. (c) We plot the predicted forces compared to ground truth for one indentation from the shear force dataset. The robot indents -0.5 N in the normal direction (green) before loading in shear (orange).

were collected synchronously for image-to-force calibration at 50 Hz and 10 Hz respectively. The time difference error between the image and force pairs was less than 0.015 s. We downsampled the force data to match the images, and collected approximately 700 (image, force) pairs per spatial point. We repeated this process for 6 random points along a 5×5 mm region of the sensor tip to create our normal force dataset over the course of several days. In total, there are 104,018 image-force pairs. We randomly split these into a training set (80k samples), validation set (10k samples), and test set (remaining 14k samples). We also prepared a much smaller subset of 10,000 randomly-selected image-force pairs with a similar split, which we refer to as “Normal (10k).”

2) *Shear Force Dataset*: For shear forces, we used a three-axis force sensor to collect the contact force vector. The procedure is similar to normal force collection at first, with an additional step of loading the probe in shear after normal force is loaded. First, the probe was controlled to apply 500 mN normal force, and then it was moved tangentially to the surface loading shear force up to 80 mN. Finally, the probe was moved back to the previous location, unloading the shear force. If there was non-zero residual shear force, we discarded the data because slip might have occurred. In total, we collected 138,348 image-force pairs over the course of several days to create our shear dataset. We randomly split this into a training set (100k samples), validation set (10k samples), and test set (remaining 28k samples). We also prepared a smaller subset of 10,000 randomly-selected image-force pairs with the same split, which we refer to as “Shear (10k).”

In training the image-to-force regression models, we used a modified ResNet-18 [48] architecture deep neural network that takes in an input image of $350 \times 350 \times 3$ and outputs a scalar output linear layer predicting the force. One early concern was that fiber-pixelated images would require significant tuning but we found that the ResNet-18 model architecture was sufficient. During training, we used mean square error as the loss and

then optimize with Adam with an initial learning rate search. The raw images from the sensor are 640×480 pixels and center-cropped and down-scaled to 350×350 pixels. We found that no other data augmentation techniques were needed for training. We used these specifications to train on the different datasets (Normal, Normal (10k), Shear, and Shear (10k)). For the shear datasets, we also learned to output the force vector direction.

We report the normal and shear force resolution in Table I, and the RMSE values in Table II. We also report a 2.6° force-angle precision for the full shear dataset, and a 3.6° force-angle precision for the smaller 10k-sample dataset. We report a median absolute error of 5 mN for the normal over unseen test sessions, and 5 mN for the shear over unseen test sessions.

Based on our results, DIGIT Pinki is able to accurately estimate light normal and shear forces over the tip of the elastomer surface. There is no significant difference in performance between the different indenter probe sizes, suggesting that DIGIT Pinki would perform well over a variety of contact sizes. The model is also able to learn comparably from both the full dataset and the smaller dataset (10k samples) for this task. In the next subsection, we also investigate an analytic model that supports the accurate force estimation performance in the light force regime.

C. Contact Area Model

Hertzian contact refers to the frictionless contact between two bodies [49], relating normal force and normal deflection at the contact interface. Given an elastomeric tactile sensor with a hemispherical tip, Hertzian contact theory may inform the expected contact area for contact with simple geometries. Although the elastomer gel is nonlinear, we expect the sensor to roughly correspond to contact mechanics theory when indented in the light force regime. Applicable to the collected indenter dataset are the contacts between a sphere and a sphere, and sphere and half-plane. In this type of contact, the

contact spot is a point contact that becomes a contact patch once the bodies deform under loading. The expressions for the circular radius of the contact patch arises from theory, which we summarize briefly below.

For the case of a sphere contacting a half-plane, the Hertzian contact radius a is given as,

$$a = \left(\frac{3FR}{4E'} \right)^{(1/3)}, \quad (2)$$

where R is the radius of the indenting sphere, F is the force with which it indents, and E' is the elastic property,

$$\frac{1}{E'} = \frac{1 - v_1^2}{E_1} + \frac{1 - v_2^2}{E_2}, \quad (3)$$

where E_1 and E_2 and the elastic moduli, and v_1 and v_2 are the Poisson's ratios for each body. For DIGIT Pinki, $E_1 \approx 0.7$ mPa and $v \approx 0.5$; the indenter is stiffer so the sensor properties dominate. For a sphere contacting a sphere, the effective radius is

$$\frac{1}{R_e} = \frac{1}{R_1} + \frac{1}{R_2}, \quad (4)$$

and for the case of a sphere contacting a flat indenter, $R_2 \rightarrow \infty$. Thus from Hertzian contact mechanics, we see that contact patch radius is proportional to cube root of the applied load F of the indenting sphere. This expected trend can be verified with image analysis from the training dataset.

We calculated the contact area radius during an indentation session from $F_z = 0$ N to -1 N with the 4 mm probe and compare this to the cube root relationship theorized in the Hertzian contact model (Fig. 7). The radius calculation was obtained by subtracting images from the no-contact baseline image, manually thresholding and contouring the resulting difference image, and determining the circle of best fit to the resulting contour. The radius is reported in pixels.

Based on our results, the Hertzian contact model trend fits closely to the observed contact area radius trend for light forces. This suggests that the gel elastic behavior is approximately linear while operating in the light force regime, which aids in learning or analytically solving for contact conditions. We note, however, that this sensor, like other rounded optical tactile sensors, will experience a reduction in sensitivity with higher loads at which the gel deformation becomes less linear and the contact patch grows more slowly. Accordingly it may be desirable to tune the sensor tip geometry to the expected geometry of an indenting object and to the anticipated load range.

V. SILICONE PALPATION EXPERIMENTS

Physical examination or palpation of tissue is regularly conducted as part of a preliminary cancer screening. During a physical exam, the clinician should be able to distinguish between the softness of healthy tissue and the comparative stiffness of cancerous tissue.

For a classification task with our sensor, we desire the ability to classify firmness over a range of values that represent both healthy and unhealthy tissue. For this, we prepared a custom dataset associating stiffness (defined as hardness values on the

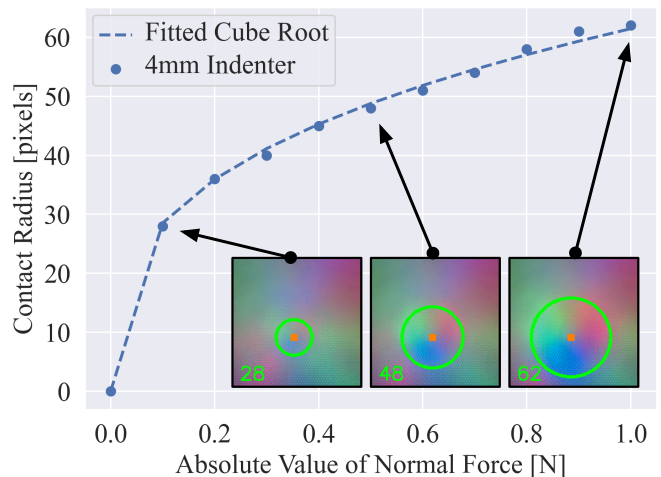


Figure 7: Comparison of actual contact area radius and expected trend as the probe indents the sensor surface with increasing force. The dashed line models the cube root fit expected with Hertzian contact. Inset are tactile images with computed radius in pixels.

Shore durometer scale for elastomers) to silicone samples of different relevant geometries. Using this dataset, we trained a classification model that classifies the hardness values based on a sequence of 16 image frames, in order to show DIGIT Pinki's potential for palpation use cases.

A. Hardness Dataset Collection

To prepare the silicone hardness dataset, we cast custom silicone samples with varied hardness values and geometries by mixing different quantities of Smooth-on Ecoflex 0050 and Smooth-On Smooth-Sil 945 platinum silicones. Ecoflex 0050 (50 Shore 00) was chosen to represent what would be considered healthy tissue, since it is reported to have a similar elastic modulus to real healthy prostate tissues from patients [50]. Smooth-Sil 945 silicone was chosen because it is significantly harder, has a fast cure time, and has a 1:1 mixing ratio that makes it easy to custom-blend different ratios. The exact mixing ratios used are detailed in the Appendix C.

We prepared molds for four different types of surfaces: flat, and with bumps of 4, 8 and 12 mm diameter, all raised 2 mm above the surface. The bump sizes were chosen based on the different diameter categories reported for lesions in prostate tissues: we desired one bump under 5 mm, one between 5 and 10 mm, and one over 10 mm. The prostate posterior is typically smooth and flat or gently concave, which the flat surface sample mimics. The flat surface sample is also used in a durometer test to find an exact hardness value for each batch.

The molds were printed with a FormLabs 3 printer using Rigid 1K resin and prepared with XTC-3D brush-on coating. We then poured the silicone mixtures into the four different molds to produce four silicone samples per batch. The samples are 7 mm thick and 25 × 25 mm across; examples are shown in Fig. 8a.

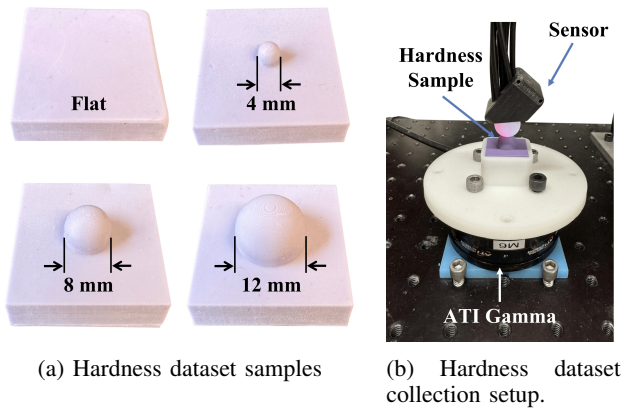


Figure 8: (a) Set of silicone samples with the same hardness value for hardness dataset. All sets of samples contain four surface types: flat, 4 mm bump, 8 mm bump, and 12 mm bump. (b) Experimental setup for collecting silicone hardness dataset. Force data was collected but not used for learning.

In total, 11 sets of silicone samples (44 individual swatches) were prepared in this manner, reflecting 11 different hardness values. The samples were randomly colored with Silc-Pig pigment (0.5% by weight) to help distinguish between them, but these addition of these colorants did not affect the hardness value. We assigned the hardness values to each sample batch by taking the average of five measurements with the durometer on the flat surface sample, where the 0.5A sample is the healthy tissue baseline.

We then used the experimental setup shown in Fig. 8b to manually palpate the silicone samples for the dataset. As shown in the figure, the samples were mounted on a 3D-printed holder that was rigidly bolted to an ATI Gamma force-torque sensor. During the palpation session, we used a computer to synchronously record both image and force data.

The palpation technique we used for the dataset collection was to manually make and break contact with the sensor tip normal to the surface of the silicone feature. We gently palpated (no more than about 2.5 N normal force) each silicone sample feature three times for one minute each, mimicking the gentleness necessary for patient comfort in a real examination. Each palpation session consisted of the raw image sequence from the tactile sensor and the forces from the ATI Gamma. We did not use the force data during model training.

B. Classification Results

To train the classification model, we first prepared the dataset—the raw RGB frames are cropped and downscaled to 224×224 pixels. To create the training, validation, and test sets we dedicated from each video frame sequence the first 80% of the frames for training and the last 20% of the frames for validation and testing. From the initial 80% of the video sequence, we create the training set by sampling from overlapping sequences of 16 frames with stride 5. Validation and test sets were created from the remaining 20% of the video sequence by sampling non-overlapping sequences of 16

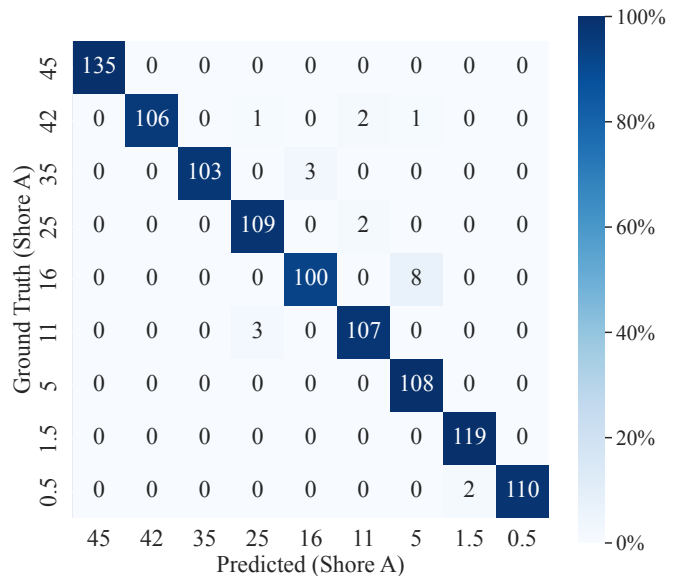


Figure 9: Classifier performance on silicone hardness class prediction task. Prediction results on the silicone hardness samples show that the learned model is capable of predicting the hardness of the samples being touched with high accuracy.

frames, where the first 10% is for validation and the remainder for test.

To perform classification, we fine-tuned transformer-based video masked autoencoders (VideoMAE) [51]. Fine-tuning was performed by training of a linear model on base model representations. The model takes as input the 16 frames sequences, and outputs a scalar that represents the hardness class. We implemented our models with PyTorch and the large instance of a pre-trained VideoMAE model openly available on HuggingFace. We used Adam optimizer with learning rate 0.005 and batch size 8, and a cross entropy loss for the classification task. The results are shown in the full confusion matrix (Fig. 9).

After evaluating the trained classification model on the test set, the model was capable of reaching 97.8% accuracy over 9 hardness classes. Based on the results, we see that the trained model performs well in classifying elastomer hardness values that correspond to the range from healthy to unhealthy tissue.

VI. PROSTATE PALPATION CASE STUDY

DIGIT Pinki provides high resolution tactile sensing that could be used to determine tissue hardness in a DRE or similar examination that would be difficult to conduct without a human finger-sized tactile sensor. We tested DIGIT Pinki in a clinically relevant task by performing palpation on phantom prostate tissue and on an *ex vivo* tissue specimen.

A. Classification of cancerous lesions in phantom prostate

We desired to test if DIGIT Pinki could make clinically relevant distinctions between cancerous lesions and healthy tissue in a prostate phantom. Six phantom prostates were first prepared by creating a mold from a patient prostate model,

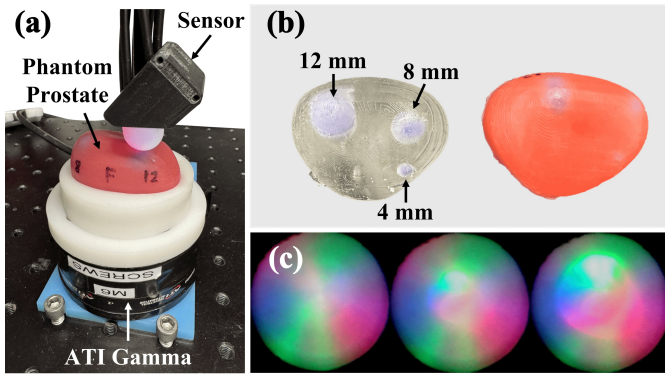


Figure 10: (a) Experimental setup for collecting phantom prostate hardness dataset. Force data was collected but not used for training. (b) (Left) A transparent phantom made from medical gel to clearly show the embedded nodules. (Right) An example of the prostate phantoms used for data collection. (c) Frames from indentation sequence on a 12 mm embedded lesion using the ungloved DIGIT Pinki tip.

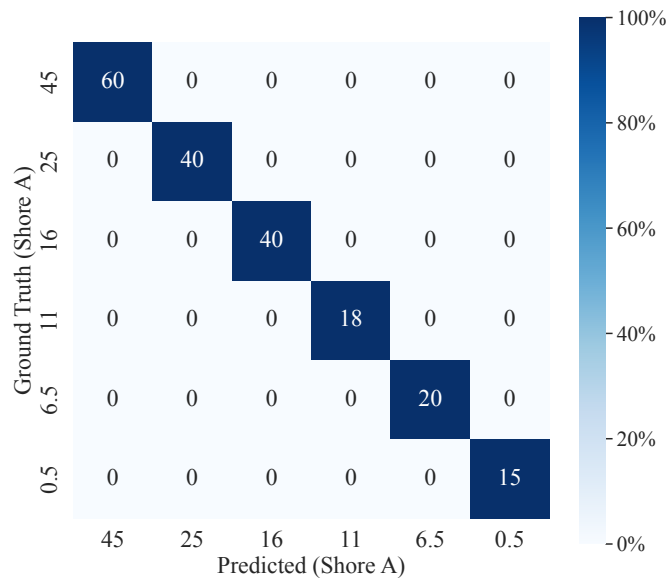


Figure 11: Classifier performance on phantom hardness class prediction task. Prediction results on the phantom hardness samples show that the model can accurately distinguish between 6 different types of nodules embedded inside the phantom.

open-sourced by the Johns Hopkins Urology Robotics Program, NCI 5R01CA247959. We selected the 41 cm² prostate model, as this was the closest size corresponding to the average volume over four radical prostatectomies that we witnessed for procedures at Stanford Hospital. We only created a mold from the posterior half, which is the portion that would be palpated in a digital rectal exam. The mold is 3D-printed using a FormLabs3 printer with Rigid 1K resin and prepared with XTC-3D brush-on finish.

We cast the healthy portion of the posterior prostate using Ecoflex 0050 (50 Shore 00), which was chosen for having a

similar elastic modulus to healthy prostate from patients [50], producing a 0.5A hardness value with a handheld durometer. We colored the Ecoflex 0050 silicone pink using 0.5% Silc-Pig red and 0.25% Silc-Pig white by weight. During the curing process, we then embedded harder spherical nodules of 4 mm, 8 mm, and 12 mm inside the phantom at a depth of 2 mm to mimic a cancerous lesion. The mixtures for the spherical nodules were mixed with the same ratios detailed in the Appendix C. The phantom prostates are fully cured at room temperature after 4 hours.

We chose to embed five different nodule hardness values inside the phantom prostates (45A, 25A, 16A, 11A, and 6.5A) to capture a range of lesion instances. As in the previously described experiment, we manually verified the hardness values of the nodules by taking the average of five measurements with a durometer from a flat silicone piece cast in the same batch as the nodule. As for the choice of hardness value for the nodules, a previous study on DRE-detectable nodules used hardness values of 23A, 27A, and 31A in simulated tissue [52], but in consultation with clinicians at Stanford Hospital who regularly perform the DRE on patients, we learned that prostate hardness values for healthy and unhealthy tissues vary widely from patient to patient. Therefore, we desired to make phantoms that reflected a wider range of possible lesion hardness values. The verisimilitude of the final phantom prostates was qualitatively assessed with clinician feedback. An example of one of the prostate phantoms is pictured in Fig. 10.

The classification experiment on the phantom tissues was conducted using data from the phantom prostate. We collected the phantom prostate data by manually palpating with DIGIT Pinki on each phantom, which was mounted atop the ATI Gamma force-torque sensor, as shown in Fig. 10. We gently palpated (with no more than 2.5 N force) over healthy phantom tissue (without an embedded nodule), and directly over each embedded nodule size. We palpated each point three times for one minute each with the usual DIGIT Pinki tip and also a tip wearing a 5 mm thick nitrile fingertip cut from the pinky finger of a small medical nitrile glove. The nitrile glove was added to simulate the nitrile glove that a clinician would wear when conducting the exam. Each session was recorded with synchronized raw video and force data although, as with the previous experiment, the forces were not used in model training.

The classifier model and parameters were set up as described in the previous experiment in Section V. We trained the classifier on the phantom palpation dataset, which included all embedded nodule sizes (4, 8, and 12 mm diameter), the six detected hardness classes (where 0.5A is the baseline healthy tissue), and palpations with a gloved sensor and an ungloved sensor. As shown in Fig. 11, we achieved a perfect accuracy score on the classification task, suggesting good performance in hardness classification on phantom prostates. We note that the classification worked well even when the sensor was gloved. Furthermore, the classification task is able to achieve respectable performance even given the different simulated lesion sizes. A human clinician might have trouble feeling the smallest 4 mm nodule during a real exam [52].

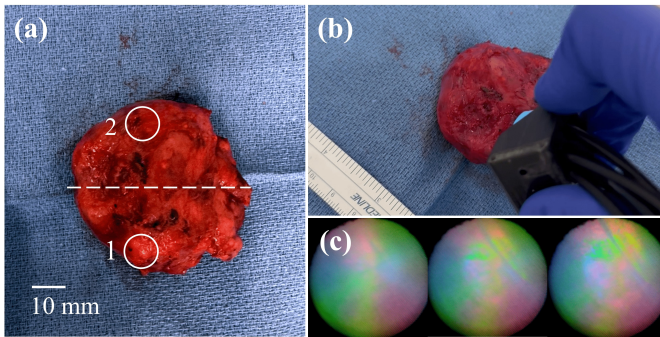


Figure 12: (a) Photo of the *ex vivo* prostate immediately after a radical prostatectomy procedure. Highlighted are the two points palpated on the posterior: the first point outlines the cancerous region, and the second point outlines the non-cancerous region. (b) Photo of manual palpation of point 1 with a gloved sensor tip. (c) Frames from an indentation sequence of point 1. The visible wrinkle is from the glove.

B. Classification of cancerous lesion in *ex vivo* prostate tissue

We brought the DIGIT Pinki to the operating room to manually palpate a resected human prostate gland immediately after a radical prostatectomy procedure. No distinction was made between tumor size, depth, or Gleason Grade of cancer when choosing to shadow this procedure. Because we palpated a fresh specimen, we mitigated the effects of the mechanical property changes that soft tissues naturally undergo when excised. The resected prostate gland is shown in Fig. 12.

This biospecimen had a Gleason Grade of 7 and was asymmetrical, where the right side contained a cancerous lesion and the left side was healthy. The attending surgeon qualitatively deemed the lesion as nonpalpable by DRE.

With a gloved DIGIT Pinki tip, the specimen was manually palpated (making and breaking contact) approximately thirty times on the posterior surface over a point on the right section (cancerous), and approximately thirty times over a symmetrical point on the left section (healthy). Data were collected over a course of six minutes. Because we had a limited amount of time with the specimen, we did not sample more points spatially.

We also manually palpated the same areas with a handheld portable durometer (Model: WonVon QMLBH0730HA-C-D). The durometer data for the point on the right side (cancerous) averaged to Shore 7.5A, and the point on the left side (non-cancerous) averaged to 5A. Because this is a handheld durometer on a specimen surface that is not entirely flat, these datapoints should only be used as a reference and not ground truth values. However, the values suggest that the hardness difference between the two points is small, reaffirming the attending surgeon’s judgement that the tumor was nonpalpable at DRE.

We trained the model, as described in Section V, on the binary classification task. This classification experiment differs from the previous one only in the creation of training, validation and test sets. Due to the small dataset, we dedicated one third of the videos for constructing the training set, one third for the validation set, and the remaining third for the

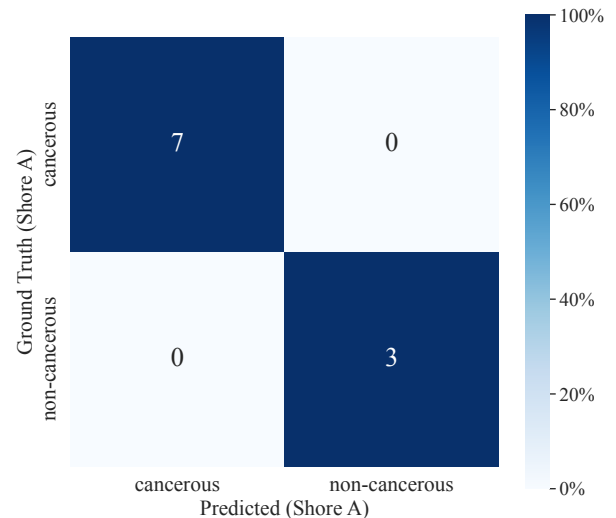


Figure 13: Classification performance on *ex vivo* prostate tissue. The experimental outcomes show that the trained model distinguished between non-cancerous and cancerous tissue in the test set.

test set. We created a training set by sampling overlapping sequences of 16 frames with stride 2. Validation and test sets were created by sampling non-overlapping sequences of 16 frames.

We measured perfect accuracy on the test set, with Fig. 13 showing the confusion matrix. Because we were only able to sample one real prostate specimen, the classification result here is of limited statistical significance. However, the result suggests that the tactile sensor is able to distinguish between the two sampled points with different stiffness values and supports the suitability and clinical relevance of DIGIT Pinki on real tissue.

VII. DISCUSSION AND FUTURE WORK

In this work, we have demonstrated a new tactile sensor design that enables miniaturization beyond that achieved by most vision-based tactile sensors. The work is motivated by a desire to create fingertips with dimensions no larger than those of human fingertips, while maintaining the spatial and force resolution that have made vision-based tactile sensing popular. The resulting sensor is suitable for manipulation and exploration tasks where space is constrained, including the palpation of human organs.

A. Future Design Directions

Ample further opportunity exists for tuning a fiber-based approach specifically to tactile sensing. One direction includes researching different fiber and microlens architectures, taking advantage of the optical customization that fibers offer. An immediate extension is to test the hyperfisheye lens design introduced in this work and to increase the fiber core count accordingly, either through purchase or by manually heating, stretching, and combining discrete fibers.

However, one does not necessarily need to use a hyperfish-eye lens to achieve a short working distance at the distal end. An interesting design direction is to replace the lens with a microlens array, producing an optical configuration akin to the compound eyes commonly found in arthropods.

Changes to the choice of imaging conduit could also be investigated. Because this work assumed that the resulting tactile images needed to be legible to humans, a coherent imaging fiber bundle was chosen. However, this is not a strict requirement for a tactile sensor, especially given the capabilities of machine learning. One may instead use a non-coherent fiber wave guide for imaging, which tends to be cheaper than coherent imaging bundles, but could increase the computation burden when training.

In addition, DIGIT Pinki could be pushed further in terms of miniaturization. For example, if all the fibers in this initial prototype were combined in a singular bundle, this design could be 8 mm in diameter or smaller, with potential uses in endoscopy. Other experiments could also tune the camera's dynamic range, exposure, and lighting to better capture details or reduce hotspots.

As became clear with the tested prototype, there is a trade-off between small size and resolution. One current drawback with a conventional fiber-based imaging system is that the number of pixels in an imaging detector (e.g., a remote CCD) is typically much greater than the number of fibers in a fiber bundle, so fiber-based imaging tends to be less sharp than a direct camera image. A related drawback is that images transmitted through fibers undergo a hexagonal sampling from the fiber packaging followed by a rectangular sampling through the imaging detector. The mismatch between essentially two sequential sampling operations leads to some data loss. To account for this, one could choose to increase the core count or use deep learning approaches to upscale or generatively fill in images. Alternatively, if an extremely small diameter is not a design priority, one can investigate a hybrid of fiber-based lighting (allowing customizable optics and mitigating heat effects at the distal end) with an endoscope "chip-on-tip" CCD imager.

B. Additional Applications

Looking further ahead, we can exploit other benefits of a fiber-based approach, such as information transfer over long distances and resistance to electromagnetic radiation, for new applications in rugged environments like in an MRI machine, underwater or in outer space. In this case, it will be necessary to retain the remote-electronics aspect of the present design.

Within the realm of medical applications, we would like to investigate other patient examinations that require understanding the tactile properties of tissue. For example, cervical tissue stiffness is an important indicator for preterm births and this sensor could be used to palpate cervical tissue to characterize stiffness. Similarly, during an open surgery of the pancreas, the surgeon will often palpate the pancreas because texture is an important predictive factor of post-operative complications. A robotic counterpart could provide repeatable quantitative measurements of texture by using a sensor like DIGIT Pinki.

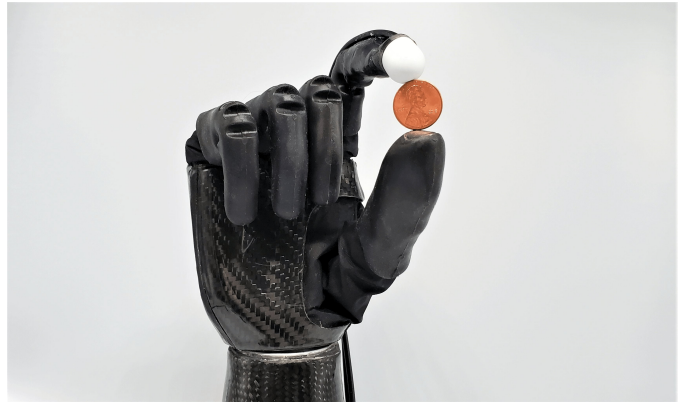


Figure 14: A concept photo showing that the compact design of DIGIT Pinki is sufficient for integration as the fingertip of a Psyonic Ability hand (holding a U.S. penny for size comparison).

A fiber-based approach is promising beyond medical applications as well. A sensitive fingertip could be integrated with a human-scale dexterous hand (Fig. 14) for tactile exploration and manipulation of delicate items. Future work could take advantage of the spatial resolution to discern object textures and forces for tasks like ripe fruit handling or cloth folding.

As a final note, we remark that the prototype presented here achieves miniaturization by virtue of moving the illumination and imaging components outside the fingertip. A consequence of this decision is that the fingertip now has space that can be reclaimed. One possible use is to add additional sensors (e.g. temperature, vibration), thereby allowing the fingertip to approximate the multimodal nature of human fingertip sensing.

VIII. CONCLUSION

As the world increasingly turns to automation to meet its needs, it is more vital than ever to empower robots with the *senses* and thereby *skills* to truly be helpful. Svelte tactile sensors will prove important for achieving human-level manipulation skill for robots, especially for tasks in constrained spaces. Towards this goal, we present a new framework for shrinking vision-based tactile sensors through the use of optical fiber bundles. We provide a proof of concept of this design philosophy with DIGIT Pinki, a compact fingertip-shaped tactile sensor that is less than the width of a fifth percentile adult male finger [11].

In this work, fundamental design considerations have been investigated for an fiber-based tactile sensor, including fiber illumination and fiber spatial resolution. The sensor image-to-force regression model shows good accuracy for a given indentation, illustrating a potential for use in closed-loop manipulation tasks in constrained environments. The image-to-hardness classification models demonstrate the potential for a miniature high-resolution tactile sensor in tissue palpation through internal orifices for patient examinations, such as for the cervix or the prostate. We open-source the design and manufacturing process of DIGIT Pinki at <https://github.com/facebookresearch/digit-design>.

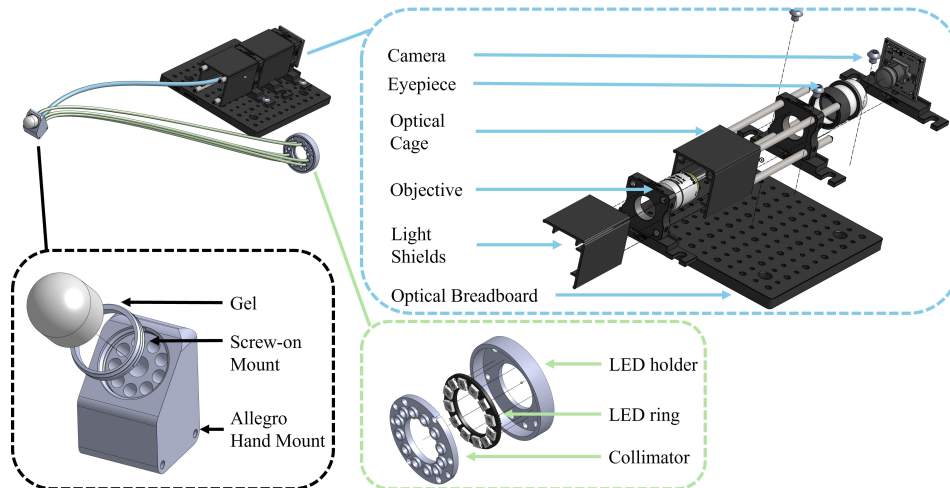


Figure 15: CAD model of the DIGIT Pinki proof of concept used in this work. Exploded views of the sensing element, imaging system, and illumination system.

While the medical applications for such a sensor are promising, we also want to acknowledge another blue-sky motivation for a slim, sensitive fingertip — to enable a more human-like fluidity and grace from robots. If robots are ever to truly enter our daily lives and be useful with their hands, they must achieve both function *and* form. In pursuit of the day when unnaturally blocky and bulky robot fingertips are no longer the standard (Fig. 14), optical fiber conduits are a promising path that we hope sparks future innovation.

ACKNOWLEDGEMENT

We thank Raymond Santos for handling administrative orders and encouragement for J.D. while at Meta, and Thomas Craven-Bartle for helpful discussions on optics theory. We thank Lee White, MD, PhD and Lori Guelman, MSN, RN, FNP-BC for helpful discussions on clinical urology practice and feedback on the prostate phantoms, and Eugene Shkolyar, MD and Geoffrey Sonn, MD for allowing J.D. to shadow several radical prostatectomy cases. We also thank Jun En Low for providing a spare Android phone for the portable DIGIT Pinki setup. The design, fabrication, and data collection of the sensor was supported through a Meta internship. This work was partly supported by the German Research Foundation (DFG, Deutsche Forschungsgemeinschaft) as part of Germany’s Excellence Strategy – EXC 2050/1 – Project ID 390696704 – Cluster of Excellence “Centre for Tactile Internet with Human-in-the-Loop” (CeTI) of Technische Universität Dresden, and by Bundesministerium für Bildung und Forschung (BMBF) and German Academic Exchange Service (DAAD) in project 57616814 (SECAI, School of Embedded and Composite AI). We thank the Zentrum für Informationsdienste und Hochleistungsrechnen (ZIH) at TU Dresden for providing computing resources.

APPENDIX A COMPLETE CAD ASSEMBLY

We provide the full CAD model for the DIGIT Pinki setup in Fig. 15.

APPENDIX B SENSOR CONSTRUCTION MANUFACTURING GUIDE

A manufacturing guide and full bill of materials is also provided at <https://github.com/facebookresearch/digit-design>.

C SILICONE PREPARATION FOR HARDNESS EXPERIMENTS

We include in Table III the mixing ratios used to achieve the silicone samples of different hardness values for this paper. After selected the desired range of hardness values, we specifically chose to use Smooth-Sil 945 and Ecoflex 0050 for manufacturing ease; they both have similar cure times and one-to-one mixing ratios between Parts A and B.

To determine the hardness value of mixed silicones, we purchased a commercial, portable Shore A durometer (Model: WonVon QMLBH0730HA-C-D) and took the average of five measurements on the flat silicone sample as the hardness value for that particular batch of samples. We report one sample as 50 on the Shore 00 scale as based on the manufacturer datasheet (the handheld Shore A scale durometer read 0.5 in manual measurements).

REFERENCES

- [1] M. Lambeta, P.-W. Chou, S. Tian, B. Yang, B. Maloon, V. R. Most, D. Stroud, R. Santos, A. Byagowi, G. Kammerer *et al.*, “Digit: A novel design for a low-cost compact high-resolution tactile sensor with application to in-hand manipulation,” *IEEE Robotics and Automation Letters*, vol. 5, no. 3, pp. 3838–3845, 2020.
- [2] W. Yuan, S. Dong, and E. H. Adelson, “Gelsight: High-resolution robot tactile sensors for estimating geometry and force,” *Sensors*, vol. 17, no. 12, p. 2762, 2017.
- [3] N. F. Lepora, “Soft biomimetic optical tactile sensing with the tactip: A review,” *IEEE Sensors Journal*, vol. 21, no. 19, pp. 21 131–21 143, 2021.

Table III: Mixing Ratios for Different Silicone Hardness

Hardness Value	Smooth-On Ecoflex 0050 (g)	Smooth-On Smooth-Sil 945 (g)
50 (Shore 00)	16	0
1.5 (Shore A)	14	2
5 (Shore A)	12	4
6.5 (Shore A)	11.5	4.5
11 (Shore A)	10	6
16 (Shore A)	8	8
20 (Shore A)	7	9
25 (Shore A)	6	10
30 (Shore A)	5	11
35 (Shore A)	4	12
42 (Shore A)	2	14
45 (Shore A)	0	16

- [4] I. H. Taylor, S. Dong, and A. Rodriguez, "Gelslim 3.0: High-resolution measurement of shape, force and slip in a compact tactile-sensing finger," in *2022 International Conference on Robotics and Automation (ICRA)*. IEEE, 2022, pp. 10 781–10 787.
- [5] S. Wang, Y. She, B. Romero, and E. Adelson, "Gelsight wedge: Measuring high-resolution 3d contact geometry with a compact robot finger," in *2021 IEEE International Conference on Robotics and Automation (ICRA)*. IEEE, 2021, pp. 6468–6475.
- [6] A. Padmanabha, F. Ebert, S. Tian, R. Calandra, C. Finn, and S. Levine, "OmniTact: A multi-directional high-resolution touch sensor," in *IEEE International Conference on Robotics and Automation (ICRA)*, 2020, pp. 618–624. [Online]. Available: <https://arxiv.org/abs/2003.06965>
- [7] M. H. Tippur and E. H. Adelson, "Gelsight360: An omnidirectional camera-based tactile sensor for dexterous robotic manipulation," in *2023 IEEE International Conference on Soft Robotics (RoboSoft)*. IEEE, 2023, pp. 1–8.
- [8] H. Sun, K. J. Kuchenbecker, and G. Martius, "A soft thumb-sized vision-based sensor with accurate all-round force perception," *Nature Machine Intelligence*, vol. 4, no. 2, pp. 135–145, 2022.
- [9] L. Wang, B. Lu, M. He, Y. Wang, Z. Wang, and L. Du, "Prostate cancer incidence and mortality: global status and temporal trends in 89 countries from 2000 to 2019," *Frontiers in Public Health*, vol. 10, p. 176, 2022.
- [10] D. S. Smith and W. J. Catalona, "Interexaminer variability of digital rectal examination in detecting prostate cancer," *Urology*, vol. 45, no. 1, pp. 70–74, 1995.
- [11] J. W. Garrett, "The adult human hand: some anthropometric and biomechanical considerations," *Human factors*, vol. 13, no. 2, pp. 117–131, 1971.
- [12] D. F. Gomes and S. Luo, "Geltip tactile sensor for dexterous manipulation in clutter," in *Tactile Sensing, Skill Learning, and Robotic Dexterous Manipulation*. Elsevier, 2022, pp. 3–21.
- [13] S. Q. Liu and E. H. Adelson, "Gelsight fin ray: Incorporating tactile sensing into a soft compliant robotic gripper," in *2022 IEEE 5th International Conference on Soft Robotics (RoboSoft)*. IEEE, 2022, pp. 925–931.
- [14] J. Zhao and E. H. Adelson, "Gelsight svelte: A human finger-shaped single-camera tactile robot finger with large sensing coverage and proprioceptive sensing," in *2023 IEEE/RSJ International Conference on Intelligent Robots and Systems (IROS)*. IEEE, 2023, pp. 8979–8984.
- [15] W. Zeng, L. Shu, Q. Li, S. Chen, F. Wang, and X.-M. Tao, "Fiber-based wearable electronics: a review of materials, fabrication, devices, and applications," *Advanced materials*, vol. 26, no. 31, pp. 5310–5336, 2014.
- [16] F. Taffoni, D. Formica, P. Saccomandi, G. Di Pino, and E. Schena, "Optical fiber-based mr-compatible sensors for medical applications: An overview," *Sensors*, vol. 13, no. 10, pp. 14 105–14 120, 2013.
- [17] C. M. Lee, C. J. Engelbrecht, T. D. Soper, F. Helmchen, and E. J. Seibel, "Scanning fiber endoscopy with highly flexible, 1 mm catheterscopes for wide-field, full-color imaging," *Journal of biophotonics*, vol. 3, no. 5-6, pp. 385–407, 2010.
- [18] A. Orth, M. Ploschner, E. Wilson, I. Maksymov, and B. Gibson, "Optical fiber bundles: Ultra-slim light field imaging probes," *Science advances*, vol. 5, no. 4, p. eaav1555, 2019.
- [19] U. H. Shah, R. Muthusamy, D. Gan, Y. Zweiri, and L. Seneviratne, "On the design and development of vision-based tactile sensors," *Journal of Intelligent & Robotic Systems*, vol. 102, pp. 1–27, 2021.
- [20] J.-S. Heo, J.-Y. Kim, and J.-J. Lee, "Tactile sensors using the distributed optical fiber sensors," in *2008 3rd International Conference on Sensing Technology*. IEEE, 2008, pp. 486–490.
- [21] H. Maekawa, K. Tanie, and K. Komoriya, "A finger-shaped tactile sensor using an optical waveguide," in *Proceedings of IEEE Systems Man and Cybernetics Conference-SMC*, vol. 5. IEEE, 1993, pp. 403–408.
- [22] S. Begej, "Planar and finger-shaped optical tactile sensors for robotic applications," *IEEE Journal on Robotics and Automation*, vol. 4, no. 5, pp. 472–484, 1988.
- [23] H. Xie, A. Jiang, H. A. Wurdemann, H. Liu, L. D. Seneviratne, and K. Althoefer, "Magnetic resonance-compatible tactile force sensor using fiber optics and vision sensor," *IEEE Sensors Journal*, vol. 14, no. 3, pp. 829–838, 2013.
- [24] B. Ali, M. A. Ayub, and H. Yusoff, "Characteristics of a new optical tactile sensor for interactive robot fingers," *International Journal of Social Robotics*, vol. 4, pp. 85–91, 2012.
- [25] H. Yusoff, J. Wada, and M. Ohka, "Sensorization of robotic hand using optical three-axis tactile sensor: Evaluation with grasping and twisting motions," *Journal of Computer Science*, vol. 6, no. 8, p. 955, 2010.
- [26] G. Zouridakis, *Biomedical technology and devices handbook*. CRC press, 2003.
- [27] S. Boppart, T. Deutsch, and D. Rattner, "Optical imaging technology in minimally invasive surgery: current status and future directions," *Surgical endoscopy*, vol. 13, pp. 718–722, 1999.
- [28] H. A. C. Wood, K. Harrington, J. M. Stone, T. A. Birks, and J. C. Knight, "Quantitative characterization of endoscopic imaging fibers," *Opt. Express*, vol. 25, no. 3, pp. 1985–1992, Feb 2017. [Online]. Available: <https://opg.optica.org/oe/abstract.cfm?URI=oe-25-3-1985>
- [29] A. R. Rouse, A. Kano, J. A. Udovich, S. M. Kroto, and A. F. Gmitro, "Design and demonstration of a miniature catheter for a confocal microendoscope," *Applied optics*, vol. 43, no. 31, pp. 5763–5771, 2004.
- [30] S. F. Elahi and T. D. Wang, "Future and advances in endoscopy," *Journal of biophotonics*, vol. 4, no. 7-8, pp. 471–481, 2011.
- [31] M. I. Tiwana, S. J. Redmond, and N. H. Lovell, "A review of tactile sensing technologies with applications in biomedical engineering," *Sensors and Actuators A: physical*, vol. 179, pp. 17–31, 2012.
- [32] W. Othman, Z.-H. A. Lai, C. Abril, J. S. Barajas-Gamboa, R. Corcelles, M. Kroh, and M. A. Qasaimeh, "Tactile sensing for minimally invasive surgery: Conventional methods and potential emerging tactile technologies," *Frontiers in Robotics and AI*, p. 376, 2022.
- [33] C. Huang, Q. Wang, M. Zhao, C. Chen, S. Pan, and M. Yuan, "Tactile perception technologies and their applications in minimally invasive surgery: a review," *Frontiers in Physiology*, vol. 11, p. 611596, 2020.
- [34] S. Wang, K. Wang, R. Tang, J. Qiao, H. Liu, and Z.-G. Hou, "Design of a low-cost miniature robot to assist the covid-19 nasopharyngeal swab sampling," *IEEE Transactions on Medical Robotics and Bionics*, vol. 3, no. 1, pp. 289–293, 2020.
- [35] S. Li, M. He, W. Ding, L. Ye, X. Wang, J. Tan, J. Yuan, and X.-P. Zhang, "Visuotactile sensor enabled pneumatic device towards compliant oropharyngeal swab sampling," *arXiv preprint arXiv:2305.06537*, 2023. [Online]. Available: <https://arxiv.org/pdf/2305.06537.pdf>
- [36] J. Konstantinova, A. Jiang, K. Althoefer, P. Dasgupta, and T. Nanayakkara, "Implementation of tactile sensing for palpation in robot-assisted minimally invasive surgery: A review," *IEEE Sensors Journal*, vol. 14, no. 8, pp. 2490–2501, 2014.
- [37] X. Jia, R. Li, M. A. Srinivasan, and E. H. Adelson, "Lump detection with a gelsight sensor," in *World Haptics Conference (WHC)*, 2013, pp. 175–179.
- [38] S. Laufer, E. R. Cohen, C. Kwan, A.-L. D. D'Angelo, R. Yudkowsky, J. R. Boulet, W. C. McGaghie, and C. M. Pugh, "Sensor technology in assessments of clinical skill," *New England Journal of Medicine*, vol. 372, no. 8, pp. 784–786, 2015.
- [39] L. Najji, H. Randhawa, Z. Sohani, B. Dennis, D. Lautenbach, O. Kavanagh, M. Bawor, L. Banfield, and J. Profetto, "Digital rectal examination for prostate cancer screening in primary care: a systematic review and meta-analysis," *The Annals of Family Medicine*, vol. 16, no. 2, pp. 149–154, 2018.
- [40] S. Bott, M. Young, M. Kellett, M. Parkinson, and C. to the UCL Hospitals' Trust Radical Prostatectomy Database, "Anterior prostate cancer: is it more difficult to diagnose?" *BJU international*, vol. 89, no. 9, pp. 886–889, 2002.
- [41] J. T. Wei, D. Barocas, S. Carlsson, F. Coakley, S. Eggner, R. Etzioni, S. W. Fine, M. Han, S. K. Kim, E. Kirkby *et al.*, "Early detection of prostate cancer: Aua/suo guideline part i: prostate cancer screening," *The Journal of Urology*, vol. 210, no. 1, pp. 46–53, 2023.
- [42] B. Ahn, H. Lee, Y. Kim, and J. Kim, "Robotic system with sweeping palpation and needle biopsy for prostate cancer diagnosis," *The Inter-*

national Journal of Medical Robotics and Computer Assisted Surgery, vol. 10, no. 3, pp. 356–367, 2014.

- [43] M. Tanaka, M. Furubayashi, Y. Tanahashi, and S. Chonan, “Development of an active palpation sensor for detecting prostatic cancer and hypertrophy,” *Smart materials and structures*, vol. 9, no. 6, p. 878, 2000.
- [44] A. Iele, A. Ricciardi, C. Pecorella, A. Cirillo, F. Ficuciello, B. Siciliano, R. La Rocca, V. Mirone, M. Consales, and A. Cusano, “Miniaturized optical fiber probe for prostate cancer screening,” *Biomedical Optics Express*, vol. 12, no. 9, pp. 5691–5703, 2021.
- [45] O. Sanni, G. Bonvicini, M. A. Khan, P. C. López-Custodio, K. Nazari *et al.*, “Deep movement primitives: toward breast cancer examination robot,” in *Proceedings of the AAAI Conference on Artificial Intelligence*, vol. 36, no. 11, 2022, pp. 12 126–12 134.
- [46] K. A. Nichols and A. M. Okamura, “Methods to segment hard inclusions in soft tissue during autonomous robotic palpation,” *IEEE Transactions on Robotics*, vol. 31, no. 2, pp. 344–354, 2015.
- [47] H. Qi, B. Yi, S. Suresh, M. Lambeta, Y. Ma, R. Calandra, and J. Malik, “General in-hand object rotation with vision and touch,” in *Conference on Robot Learning (CORL)*, 2023. [Online]. Available: <https://arxiv.org/abs/2309.09979>
- [48] K. He, X. Zhang, S. Ren, and J. Sun, “Deep residual learning for image recognition,” in *Proceedings of the IEEE conference on computer vision and pattern recognition*, 2016, pp. 770–778.
- [49] H. Hertz, “Über die berührung fester elastischer körper,” *J reine und angewandte Mathematik*, vol. 92, p. 156, 1881.
- [50] S. E. Navarro, S. S. Dhaliwal, M. S. Lopez, S. Wilby, A. L. Palmer, W. Polak, R. Merzouki, and C. Duriez, “A bio-inspired active prostate phantom for adaptive interventions,” *IEEE Transactions on Medical Robotics and Bionics*, vol. 4, no. 2, pp. 300–310, 2021.
- [51] Z. Tong, Y. Song, J. Wang, and L. Wang, “Videomae: Masked autoencoders are data-efficient learners for self-supervised video pre-training,” *Advances in neural information processing systems*, vol. 35, pp. 10 078–10 093, 2022.
- [52] L. A. Baumgart, G. J. Gerling, and E. J. Bass, “Characterizing the range of simulated prostate abnormalities palpable by digital rectal examination,” *Cancer epidemiology*, vol. 34, no. 1, pp. 79–84, 2010.

BIOGRAPHY SECTION



Julia Di received the B.S. degree in Electrical Engineering with a minor in Computer Science from Columbia University, New York, NY, USA in 2018. She received the M.S. in Mechanical Engineering from Stanford University, Stanford, CA, USA in 2020. Her research interests include tactile sensing, sensor networks, and perception of grasping.



Zdravko Dugonjic received the MSc degree in Computer Science from Université Grenoble Alpes in 2023. He is a Ph.D. student in Learning, Adaptive Systems, and Robotics (LASR) Lab, at Technische Universität Dresden. His research interests are touch perception and machine learning.



Will Fu received a Bachelor Degree in Computer Science and a Bachelor Degree in Business from Nanyang Technological University in 2017. His research interests are computer vision for robotics and deep learning recommendation models.



Tingfan Wu received the Ph.D. degree in Computer Science from University of California, San Diego, San Diego, CA, USA in 2013. Dr. Wu is currently a Research Engineer at Meta, Menlo Park, CA, USA. His research interests include machine learning and robotics.



Romeo Mercado received the Ph.D. degree in Optical Science from University of Arizona in 1973. Dr. Mercado is an optical scientist and consultant with over 30 years of experience in optics. He holds 35 U.S. patents and a number of foreign patents on optical system designs.



Kevin Sawyer received the Ph.D. degree in Engineering Mechanics from the University of Arizona in 1995. Dr. Sawyer is a senior optomechanical engineer and adjunct professor at San Jose State University, with over 30 years of experience in optoelectronics.



Victoria Rose Most received the B.A. in Animation from the College for Creative Studies in 2007. She is currently a Design Model Maker at Meta, Menlo Park, CA, USA. She has over 15 years of experience in silicone molding and casting in the entertainment industry, including *Coraline* (2009).



Gregg Kammerer received the B.S. degree in Law Enforcement and Justice Administration from Western Illinois University in 1994. He has 30 years of experience as a model maker and machinist prototyper.



Stefanie Speidel (Senior Member, IEEE) received the Ph.D. (Dr.Ing.) degree from the Karlsruhe Institute of Technology (KIT), Karlsruhe, Germany, in 2009. She has been a Professor for “Translational Surgical Oncology” at the National Center for Tumor Diseases (NCT/UCC) Dresden, Dresden, Germany, since 2017, and a Deputy Speaker of the DFG Cluster of Excellence “Centre for Tactile Internet with Human-in-the-Loop” (CeTI) since 2019 and the Konrad Zuse AI school SECAI since 2022.



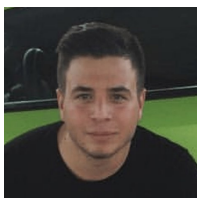
Richard E. Fan received the Ph.D. degree in biomedical engineering from University of California, Los Angeles in 2010. Dr. Fan is currently the Engineering Director of the Urologic Cancer Innovation Lab and a Clinical Assistant Professor in Urology at Stanford University.



Geoffrey Sonn, MD is a board certified urologist who specializes in treating patients with prostate and kidney cancer. Dr. Sonn has a particular interest in cancer imaging, MRI-Ultrasound fusion targeted prostate biopsy, prostate cancer focal therapy, and robotic surgery for prostate and kidney cancer. He is a member of Stanford Bio-X, the Stanford Cancer Institute, and Associate Member of the Canary Center at Stanford for Cancer Early Detection.



Mark R. Cutkosky received the Ph.D. degree in mechanical engineering from Carnegie Mellon University, Pittsburgh, PA, USA in 1985. He is the Fletcher Jones Professor in Mechanical Engineering at Stanford University, Stanford, CA, USA. His research interests include bioinspired robots, haptics, and rapid prototyping processes. Dr. Cutkosky is a Fellow of IEEE and ASME.



Mike Lambeta is an AI Research Engineer in Hardware at Meta, Menlo Park, CA, USA. His research interests include tactile sensing and robotics.



Roberto Calandra is a Full (W3) Professor at the Technische Universität Dresden, and at the Centre for Tactile Internet with Human-in-the-Loop (CeTI). Previously, he founded at Meta AI (formerly Facebook AI Research) the Robotic Lab in Menlo Park. Prior to that, he was a Postdoctoral Scholar at the University of California, Berkeley (US) in the Berkeley Artificial Intelligence Research (BAIR) Lab. His education includes a Ph.D. from TU Darmstadt (Germany), a M.Sc. in Machine Learning and Data Mining from the Aalto university (Finland), and a B.Sc. in Computer Science from the Università degli studi di Palermo (Italy). His scientific interests are broadly at the conjunction of Robotics and Machine Learning, with the goal of making robots more intelligent and useful in the real world. Among his contributions is the design and commercialization of DIGIT – the first commercially available high-resolution compact tactile sensor. Roberto served as Program Chair for AISTATS 2020, as Guest Editor for the JMLR Special Issue on Bayesian Optimization, and has previously co-organized over 16 international workshops (including at NeurIPS, ICML, ICLR, ICRA, IROS, RSS).